ADVANCED OPTICAL MATERIALS
www.advopticalmat.de

Optical Vortex Transmutation with Geometric Metasurfaces of Rotational Symmetry Breaking

Yuchao Zhang, Jie Gao, and Xiaodong Yang**

The free-space optical vortex transmutation is realized by using geometric plasmonic metasurfaces with the designed noncanonical vortex phase profiles possessing discrete rotational symmetries of finite order. Based on the introduced continuous-to-discrete rotational symmetry breaking in metasurfaces, the vortex transmutation phenomena are observed behind the metasurfaces from the near-field to far-field diffraction in free space. The near-field optical beam profile represents the input vortex, while in the far field the input vortex is diffracted into the central output vortex with topological charge determined by the transmutation rule and the symmetrically distributed off-axis vortices with unity topological charge bifurcating from the input vortex, with the total orbital angular momentum conserved. The demonstrated free-space optical vortex transformation will promise many potential applications related to optical communication, particle manipulation, and quantum information processing.

1. Introduction

Optical vortices carrying phase singularities and orbital angular momentum (OAM) have unique characteristics of intensity, phase, and energy flows, which play important roles in many scientific fields ranging from classic optics to quantum physics, such as optical trapping,[1–3] optical communication,[4,5] quantum information,[6–10] spin-orbit interaction,[11,12] and Bose–Einstein condensates.[13,14] An optical vortex has a helical phase structure with azimuthal phase dependency of $\exp(il\varphi)$, where φ is the azimuthal angle and l is vorticity or topological charge (TC) of the vortex. As the most essential parameter, l represents the phase increase around the singularity and $l\hbar$ represents the OAM per photon. It has been proved that the vorticity l should be conserved in free space with $O(2)$ continuous rotational symmetry.[15] However, if a medium has the symmetry breaking from $O(2)$ continuous symmetry into C_N discrete rotational symmetry of Nth order, the vorticity conservation is not preserved and the vortex transmutation phenomenon is observed.[16–26] Many previous works have been done to show the vortex transmutation rule by using photonic lattices or diffractive optical elements with C_N discrete symmetry.[20–26] By using polygonal lenses as diffractive optical elements, the free-space vortex transmutation has been realized for changing the central vorticity of a coaxially incident optical vortex.[22–26] Recently, the free-space vortex transmutation has also been observed in the vortex generation by the closed-path nanoslits, where the TC of output central vortex is limited by the discrete symmetry of arc-shaped nanoslit.[27]

The common diffractive optical elements such as polygonal lenses and spatial light modulators realize phase modulations based on optical path difference, which have bulky size and are limited by the material dispersion. To overcome the bandwidth limitation, the geometric metasurfaces have been used to effectively tailor the phase and polarization of light,[28–33] where the phase change originates from the geometric phase that accompanies polarization conversion rather than optical path difference, so that the metasurfaces could operate in a broadband wavelength range. The geometric metasurfaces provide a compact and effective approach in building the integrated wave-front shaping devices such as vortex beam converters,[34–37] flat optical lenses,[38–43] ultrathin wave plates,[44–47] and multiplexed holograms.[48–52]

Here, the geometric plasmonic metasurfaces with noncanonical vortex phase structures are designed as a new approach to realize the free-space optical vortex transmutation. By modulating the helical phase fronts with azimuthal nonlinear semicircle functions having C_N discrete rotational symmetries, the $O(2)\rightarrow C_N$ continuous-to-discrete rotational symmetry breaking is introduced into the metasurfaces, which results in the observation of the vortex transmutation phenomena behind the metasurfaces from the near-field to far-field diffraction in free space. At the near field, the input vortex is generated right behind the metasurface showing the specified TC. In the far field, the transmuted central output vortex with topological charge determined by the transmutation rule is observed, together with the symmetrically distributed off-axis vortex clusters with unity topological charge bifurcating from the input vortex. Meanwhile, since the whole system is placed in free space and no external vorticity is introduced, it is found that the total OAM is conserved. The demonstrated free-space optical vortex transformation will lead to many promising applications in optical communication, particle manipulation, and quantum information processing.

Dr. Y. Zhang, Prof. J. Gao, Prof. X. Yang
Department of Mechanical and Aerospace Engineering
Missouri University of Science and Technology
Rolla, MO 65409, USA
E-mail: gaojie@mst.edu; yangxia@mst.edu
The ORCID identification number(s) for the author(s) of this article can be found under https://doi.org/10.1002/adom.201901152.

DOI: 10.1002/adom.201901152

© 2019 WILEY-VCH Verlag GmbH & Co. KGaA, Weinheim

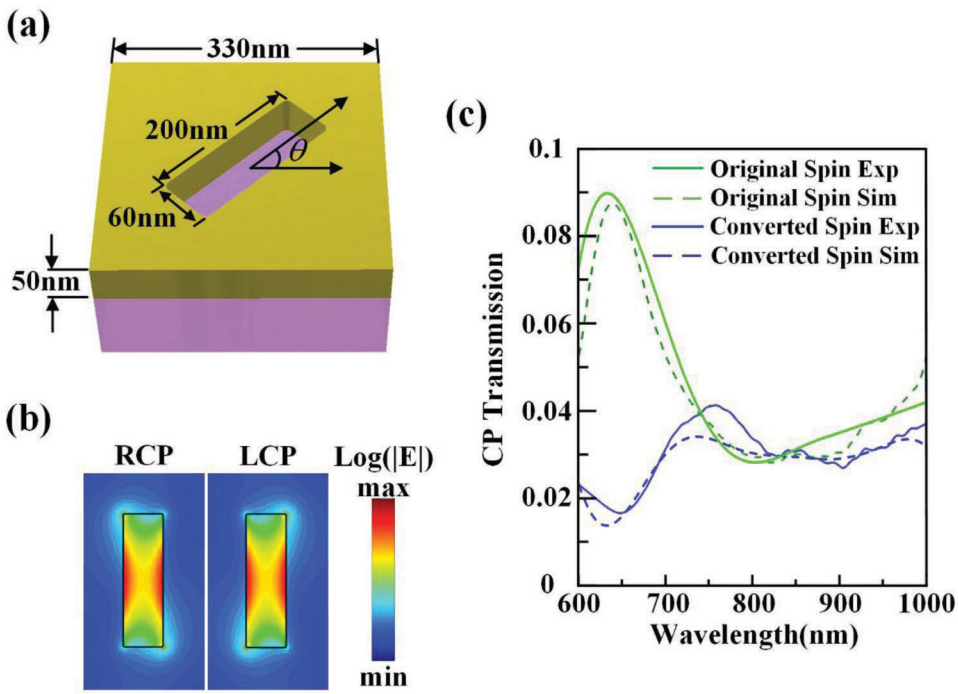

Figure 1. a) Schematic of the unit cell with nanoslit antenna at orientation angle θ. b) Simulated electric field $|E|$ distributions of nanoslit antenna under circular polarizations at 633 nm. c) Measured and simulated transmission spectra under circular polarizations.

2. Results and Discussion

2.1. Design of Geometric Metasurface

The geometric metasurface is constructed from the nanoslit antenna array fabricated in a thin gold film with a thickness of 50 nm on a glass substrate by focused ion beam (FIB) method. As shown in **Figure 1**a, the width and length of each nanoslit antenna are 60 and 200 nm, respectively, and the unit cell period is 330 nm. As the circularly polarized light transmits through the nanoslit, the converted spin component will get the geometric phase shift of 2θ, with θ as the orientation angle of nanoslit. The designed geometric phase profile of the metasurface is realized by rotating the nanoslit antennas with certain angles in a spatially inhomogeneous array. Figure 1b shows the simulated electric field distributions for the right-handed and left-handed circular polarizations (RCP and LCP), which exhibit strong polarization anisotropy. Figure 1c plots the measured and simulated transmission spectra of original (LCP) and converted (RCP) spin components. The original spin transmission is defined as the intensity ratio between the transmitted LCP component and the incident LCP beam, while the converted spin transmission is defined as the intensity ratio between the converted RCP component and the incident LCP beam. The converted spin transmission through the nanoslit antennas is around 2–4%. It has been known that the low transmission efficiency from the discretely shaped plasmonic metasurfaces is due to the large Ohmic loss of metal and the discrete wavefront, which will lead to a low signal-to-noise ratio.[53] In order to overcome such limitation, quasi-continuous metasurfaces made of catenary apertures have recently been proposed to achieve high achromatic polarization conversion efficiency and improve the operating bandwidth.[54] Continuously shaped metasurfaces have also been studied to get low phase noise and high polarization conversion efficiency.[53]

The noncanonical vortex phase profile possessing C_N discrete rotational symmetry is employed to realize the optical vortex transmutation. For the normal canonical vortex structure, the helical phase structure has linearly increased phase along the azimuthal direction around the vortex center. However, for the noncanonical vortex phase structure, the helical phase structure is superimposed with an extra azimuthal nonlinear phase. For example, the TC inversion process has been demonstrated upon using the noncanonical vortex phase structure based on the phase variation from the single-charge canonical vortex.[55,56] Topological shaping of light has been realized by using the closed-path nanoslits consisting of multiple circular arcs with the azimuthal nonlinear phase modulation.[27] Modulated optical vortices have been generated by including a sinusoidal or tangential modulation factor in the azimuthal nonlinear phase profile.[57,58] In this work, the noncanonical vortex phase profile is constructed by modulating the helical phase front with azimuthal nonlinear semicircle function having C_N discrete rotational symmetry, as the following steps. With the selected C_N discrete rotational symmetry with Nth order, where $N = 3$, 5 or 8, the initial input phase plane is divided into N parts azimuthally with the corresponding angle of $2\pi/N$ for each part, as shown in **Figure 2**a. Then, an azimuthal nonlinear semicircle phase function P_{non} is introduced with P_{non}^{k} for the kth part, which can be expressed as

$$P_{\text{non}}^{k} = \sqrt{\left(\frac{\pi}{N}\right)^2 - \left(\phi - \frac{k\pi}{N}\right)^2}, \quad \text{with} \quad \frac{2\pi(k-1)}{N} < \phi < \frac{2\pi k}{N} \tag{1}$$

© 2019 WILEY-VCH Verlag GmbH & Co. KGaA, Weinheim

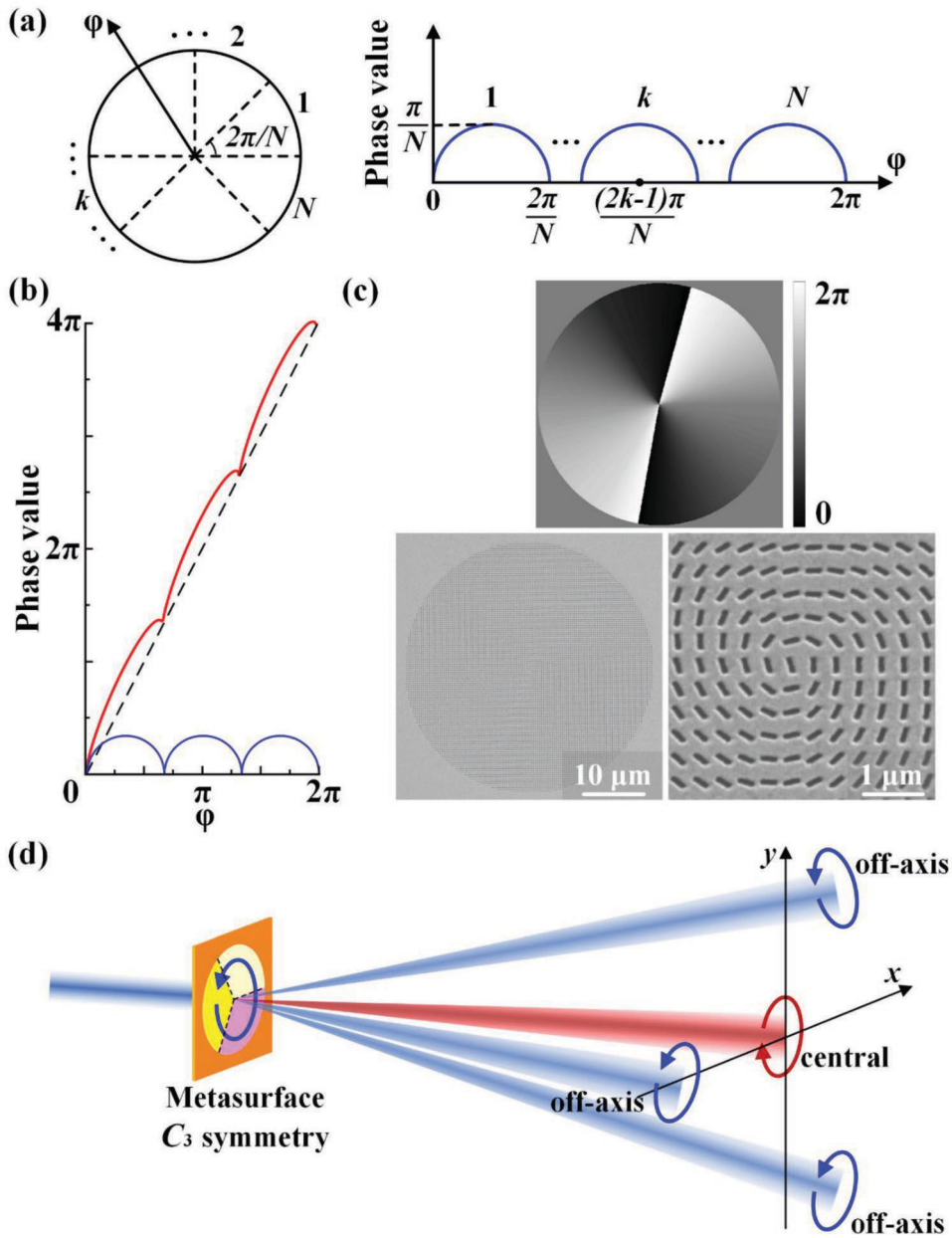

Figure 2. a) Generation of azimuthal nonlinear semicircle phase function with C_N discrete rotational symmetry. b) The noncanonical vortex phase profile along the azimuthal direction for $N = 3$ and $l_{in} = 2$. c) The noncanonical vortex phase profile encoded on the metasurface and the SEM image of the fabricated metasurface corresponding to (b). d) Schematic of the free-space optical vortex transmutation through the near-field to far-field diffraction. In the far field, the transmuted central vortex is marked as red and the surrounding off-axis vortices are marked as blue.

$$P_{non} = \sum_{k=1}^{N} P_{non}^{k} \tag{2}$$

where φ is the azimuthal angle. Finally, the total noncanonical vortex phase profile is obtained by adding P_{non} into the helical phase structure exp $(il_{in}\varphi)$ of the input vortex, which gives the geometric phase profile encoded onto the metasurface

$$P_{geom}(\varphi) = l_{in}\varphi + P_{non} \tag{3}$$

The rotation angle θ of the nanoslit antenna in each unit cell is then determined by $\theta = P_{geom}/2$. For the case of $(N, l_{in}) = (3, 2)$, the azimuthal phase profile is shown in Figure 2b, where the blue solid line is the azimuthal nonlinear semicircle function P_{non} with C_N discrete symmetry, the black dashed line represents the helical phase structure exp $(i2\varphi)$ of the input vortex, and the red solid line is the total noncanonical vortex phase profile P_{geom} along the azimuthal direction. It is noted that the designed noncanonical vortex phase profile only has the azimuthal dependence, which is different from the phase functions of polygonal lenses and arc-shaped nanoslits with both the azimuthal and radial dependence. Figure 2c displays the corresponding noncanonical vortex phase profile and its SEM image of the fabricated metasurface.

© 2019 WILEY-VCH Verlag GmbH & Co. KGaA, Weinheim

According to the vortex transmutation rule, for the medium with C_N discrete rotational symmetry, the relationship between the input vortex TC l_{in} and the transmuted TC of output vortex l_T can be expressed as

$$l_T = l_{in} - qN, \text{ with } q \in \mathbb{Z} \tag{4}$$

which is based on the fulfilled condition of $\exp[i(l_{in} - l_T)2\pi/N] = 1$ and q is an integer.[16] q is the cutoff index which represents the change of OAM when the vortex is transmuted form $O(2)$ symmetry into C_N discrete rotational symmetry. And l_T also satisfies the cutoff condition of $|l_T| < N/2$ (for even N) or $|l_T| \leq (N-1)/2$ (for odd N). The vortex transmutation rule along with the cutoff condition will univocally determine the transmuted TC l_T and the integer q. As an example, for the case of $(N, l_{in}) = (3, 5)$, the vortex transmutation rule gives $l_T = +2$ if $q = 1$ and $l_T = -1$ if $q = 2$, but the cutoff condition requires $|l_T| \leq 1$, so that the values of $l_T = -1$ and $q = 2$ are finally determined. As illustrated in Figure 2d, the $O(2) \rightarrow C_N$ rotational symmetry breaking introduced into the metasurface will result in the free-space optical vortex transmutation behind the metasurface through the beam diffraction. At the near field, the input vortex with the specified TC l_{in} is generated, while the far-field output contains the transmuted central vortex with TC l_T and q sets of symmetrically distributed off-axis vortex clusters with each cluster made of N unity-TC vortices emanating from the center. Since the system is placed in free space and no external vorticity is introduced, the total output vortex TCs will fulfill the OAM conservation rule, which is consistent with the vortex transmutation rule shown in Equation (4).

2.2. Free-Space Optical Vortex Transmutation

The free-space optical vortex transmutation is realized by the near-field to far-field diffraction behind the geometric metasurface encoded with the designed noncanonical vortex phase profile. Here five cases with different C_N discrete symmetries and input vortex TCs are considered with $(N, l_{in}) = \{(3, 2); (3, 3); (3, 5); (5, 3); (8, 5)\}$, and the corresponding transmuted TCs can be calculated by Equation (4) as $l_T = \{-1, 0, -1, -2, -3\}$ with $q = \{1, 1, 2, 1, 1\}$, respectively. The numerical simulation is first performed by using the Fresnel–Kirchhoff diffraction formula. The intensity and phase distributions at the near-field position $z = 1$ mm and the far-field position $z = 5$ cm behind the metasurfaces are calculated, as shown in **Figure 3**. Figure 3a displays the designed noncanonical vortex phase profiles given by Equation (3) for all five cases, showing the helical phase structure corresponding to each input vortex TC l_{in}. The near-field intensity and phase distributions at $z = 1$ mm are plotted in Figure 3b,c, respectively. The intensity profile at the near field give a donut shape around the dark core at the beam center and the size of donut shape increases as the input vortex TC l_{in} increased. Besides, each intensity profile also contains a slight perturbation modulated with C_N discrete rotational symmetry. The phase profile at the near field has the helical phase structure with the same TC as the input vortex TC l_{in}. Figure 3d,e shows the calculated far-field intensity and phase profiles at $z = 5$ cm. The intensity profile in the far field gives a pattern with C_N discrete rotational symmetry. For the case of $(N, l_{in}) = (3, 2)$, the intensity has a C_3-symmetric distribution with a triangle-shaped dark core. And the corresponding phase distribution exhibits four vortices, including one transmuted on-axis vortex located at the beam center (marked by the yellow arrow) and three other off-axis vortices symmetrically distributed around the beam center (marked by the white arrows). The transmuted central vortex has clockwise-increased helical phase with TC of $l_T = -1$, and the three off-axis vortices have counterclockwise-increased helical phase with TC of +1, which satisfies the vortex transmutation rule of Equation (4) with $N = 3$ and $q = 1$. The total output vortex TC of +2 is also equal to the input vortex TC, satisfying the total OAM conservation rule. For the case of $(N, l_{in}) = (3, 3)$, it shows that the intensity has C_3 symmetry but there is no vortex structure at the beam center with $l_T = 0$, which is also indicated by the phase profile, while three off-axis vortices with TC of +1 are distributed surrounding the center. For the case of $(N, l_{in}) = (3, 5)$, there is one transmuted central vortex with TC of −1 and two sets of off-axis vortex clusters with three vortices of TC = +1 in each cluster, with $q = 2$ in Equation (4). These two off-axis vortex clusters are trigonally distributed around the center, with one cluster near the center and another cluster away from the center. For the case of $(N, l_{in}) = (5, 3)$, the intensity has C_5 symmetry with a pentagonal dark core. The phase profile shows the central vortex with TC of −2 and five off-axis vortices with TC of +1 pentagonally distributed around the center. For the case of $(N, l_{in}) = (8, 5)$, the intensity shows C_8 symmetry with an octagonal dark core. The phase profile gives the on-axis vortex with TC of −3 and eight off-axis vortices with TC of +1 around the center. It can be seen that the vortex transmutation rule is satisfied for all the five cases and the total OAM conservation is also fulfilled. The distribution of N off-axis vortices for each vortex cluster exhibits C_N discrete symmetry with q sets of vortex clusters. For the case $q = 1$, one set of N off-axis vortices are distributed along one circle surrounding the center, while for $q = 2$ there are two sets of N off-axis vortices with one set distributed in the inner circle and the other set distributed in the outer circle around the center, as shown in Figure 3e for the case of $(N, l_{in}) = (3, 5)$.

Next, the optical vortex transmutation phenomena are observed in experiments with the fabricated geometric metasurfaces at the wavelength of 633 nm. **Figure 4** displays the measured intensity distributions and interference patterns at the near-field position $z = 1$ mm and the far-field position $z = 5$ cm behind the metasurfaces, which are captured by a microscope imaging system with a 20 × objective lens, a 0.5 × tube lens and a charge-coupled device (CCD) camera placed on a translation stage. The interference patterns are measured with a Mach-Zehnder interferometer, where the vortex beam is interfered with a spherical wave under the certain circular polarization, and the vortex TC can be obtained from the number of interference spirals. Figure 4a gives the near-field intensity distributions for the five cases, presenting the donut shape around the dark core at the beam center and the l_{in}-dependent size of donut shape. Figure 4b plots the corresponding near-field interferometry patterns showing counterclockwise-rotated spirals located at the beam center, where the number of spirals is equal to the input vortex TC l_{in}. Figure 4c gives the far-field intensity profiles with C_N symmetry, which are coincident with

© 2019 WILEY-VCH Verlag GmbH & Co. KGaA, Weinheim

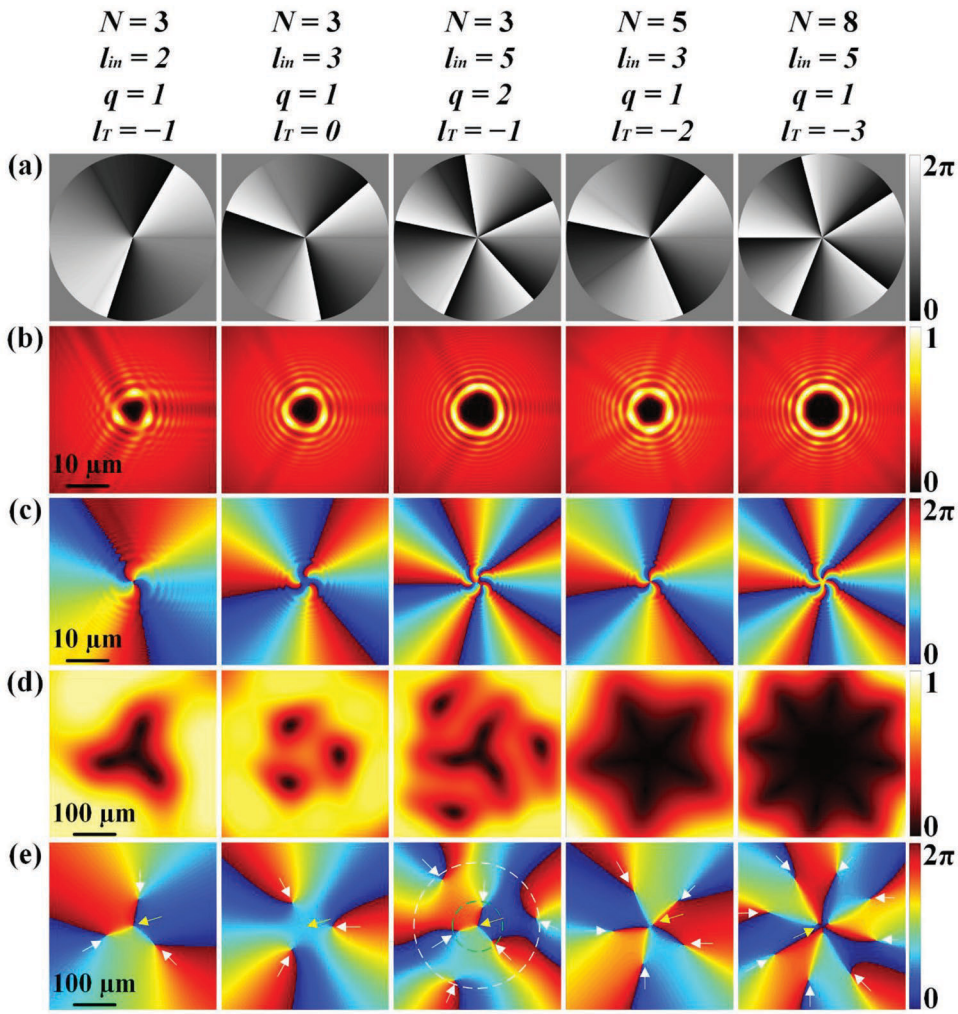

Figure 3. a) The designed noncanonical vortex phase profiles for five cases of $(N, l_{in}) = \{(3, 2); (3, 3); (3, 5); (5, 3); (8, 5)\}$. b,c) The calculated near-field intensity and phase distributions. d,e) The calculated far-field intensity and phase profiles. The yellow arrows in (e) mark the transmuted central vortices and the white arrows mark the surrounding off-axis vortices. For the case of $(N, l_{in}) = (3, 5)$ in (e), the green and white dashed circles represent the locations of the two sets of off-axis vortex clusters with C_3 symmetry.

the simulation results. The far-field interference patterns in Figure 4d shows the interference spirals of both the transmuted central vortex (marked by the yellow arrows) and the off-axis vortices distributed surrounding the center (marked by the white arrows). For the case of $(N, l_{in}) = (3, 2)$, there is one spiral with clockwise rotation at the beam center, indicating $l_T = -1$ for the transmuted central vortex. While there are three spirals with counterclockwise rotation trigonally distributed around the center, indicating three off-axis vortices with TC = +1. For the case of $(N, l_{in}) = (3, 3)$, there is no spiral in the center with $l_T = 0$ and three spirals representing three off-axis vortices with TC = +1 appear. For the case of $(N, l_{in}) = (3, 5)$, one clockwise-rotated spiral appears in the beam center, indicating the transmuted central vortex has $l_T = -1$. While there are six counterclockwise-rotated spirals around the beam center, representing the two sets of off-axis vortex clusters with each cluster made of three vortices with TC = +1. For the case of $(N, l_{in}) = (5, 3)$ or $(N, l_{in}) = (8, 5)$, two or three clockwise-rotated spirals appear at the beam center indicating $l_T = -2$ or -3, while five or eight counterclockwise-rotated spirals distribute around the center, showing the five or eight off-axis vortices with TC = +1. All the interference results agree with the simulated phase profiles, manifesting the vortex transmutation rule and OAM conservation rule for all the cases.

3. Conclusion

In summary, the free-space optical vortex transmutation is demonstrated by using the geometric plasmonic metasurfaces with the designed noncanonical vortex phase profiles. The $O(2) \rightarrow C_N$ symmetry breaking is introduced to the metasurfaces by modulating the helical phase fronts with azimuthal nonlinear semicircle functions having C_N discrete rotational symmetries. The optical vortex transmutation is observed behind the metasurfaces from the near-field to far-field diffraction. The input vortex is generated at the near field, while the transmuted central vortex and the off-axis vortex clusters are observed in the

© 2019 WILEY-VCH Verlag GmbH & Co. KGaA, Weinheim

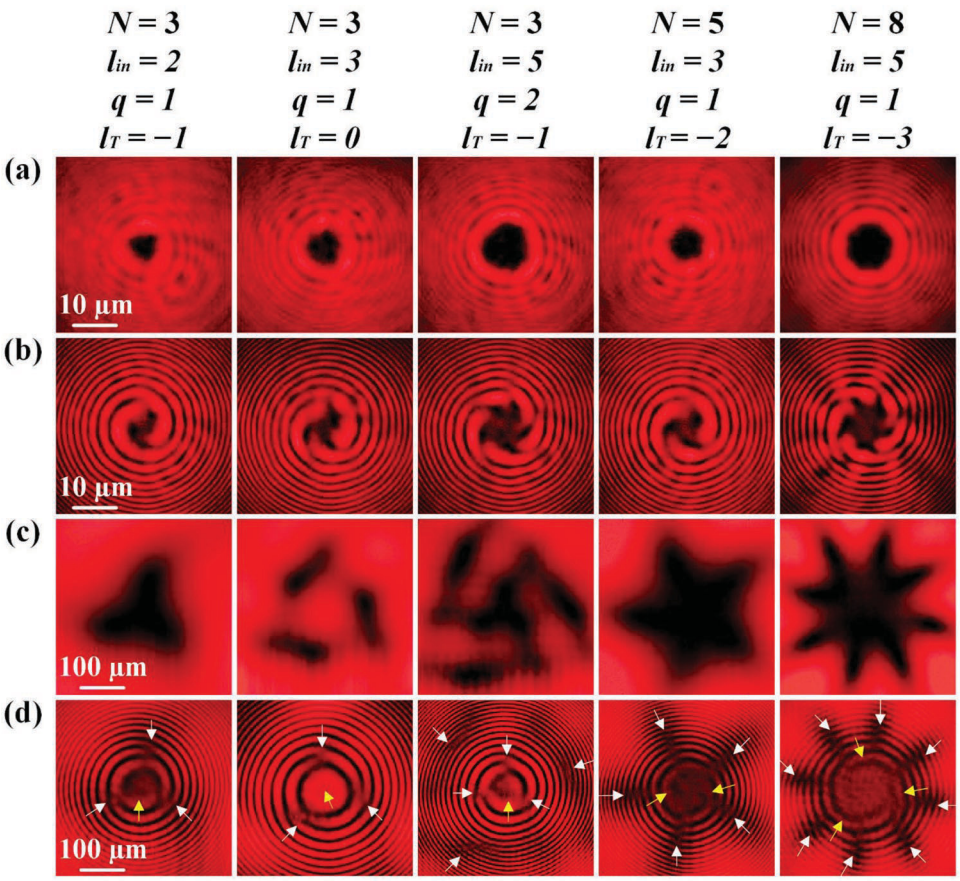

Figure 4. a,b) The measured near-field intensity distributions and interference spiral patterns. c,d) The measured far-field intensity profiles and interference spiral patterns. The yellow arrows in (d) mark the interference spirals of the transmuted central vortices and the white arrows mark the interference spirals of the surrounding off-axis vortices.

far field, where the input TC, transmuted TC, and the number of off-axis vortices with unity TC satisfy the vortex transmutation rule with the total OAM conserved. The demonstrated free-space optical vortex transformation will advance a variety of promising applications in particle manipulation and transportation, quantum information processing, and OAM-multiplexed optical communication.

4. Experimental Section

Numerical Simulation: The CST Studio Suite software was employed to simulate the electric field distributions and transmission spectra in Figure 1 with periodic boundary conditions in the unit cell. The near-field and far-field intensity and phase distributions of vortex transmutation in Figure 3 were calculated with the Fresnel–Kirchhoff diffraction integral.[59]

Sample Fabrication: Gold film with a thickness of 50 nm was deposited on a glass slide with electron-beam evaporation. The nanoslit antennas were milled with focused ion beam (30 kV, 9.7 pA). The metasurface had 150 × 150 unit cells with nanoslit antennas at the designed orientation angles.

Optical Characterization: The transmission spectra in Figure 1c were measured with a white light source and a spectrometer. The circularly polarized light was obtained through a linear polarizer and a quarter-wave plate. A HeNe laser at the wavelength of 633 nm was used in the measurements in Figure 4. The intensity profiles and interferometry patterns of optical vortices were imaged by a microscope system with a CCD camera.[59]

Acknowledgements

The authors acknowledge support from the Office of Naval Research under Grant No. N00014-16-1-2408 and the National Science Foundation under Grant Nos. ECCS-1653032 and DMR-1552871. The authors thank the facility support from the Materials Research Center at Missouri S&T.

Conflict of Interest

The authors declare no conflict of interest.

Keywords

geometric phase, metasurfaces, orbital angular momentum, vortex transmutation

Received: July 9, 2019
Revised: August 7, 2019
Published online: August 23, 2019

[1] D. Grier, *Nature* **2003**, *424*, 810.
[2] R. P. Lopez, U. Ruiz, V. Arrizon, R. R. Garcia, *Opt. Lett.* **2016**, *41*, 4138.
[3] M. Padgett, R. Bowman, *Nat. Photonics* **2011**, *5*, 343.

 © 2019 WILEY-VCH Verlag GmbH & Co. KGaA, Weinheim

[4] J. Wang, J. Y. Yang, I. M. Fazal, N. Ahmed, Y. Yan, H. Huang, Y. Ren, Y. Yue, S. Dolinar, M. Tur, A. E. Willner, *Nat. Photonics* **2012**, *6*, 488.
[5] P. J. Winzer, *Nat. Photonics* **2014**, *8*, 345.
[6] R. Fickler, R. Lapkiewicz, M. Huber, M. P. Lavery, M. J. Padgett, A. Zeilinger, *Nat. Commun.* **2014**, *5*, 4502.
[7] A. Nicolas, L. Veissier, L. Giner, E. Giacobino, D. Maxein, J. Laurat, *Nat. Photonics* **2014**, *8*, 234.
[8] A. Mair, A. Vaziri, G. Weihs, A. Zeilinger, *Nature* **2001**, *412*, 313.
[9] R. Fickler, R. Lapkiewicz, W. N. Plick, M. Krenn, C. Schaeff, S. Ramelow, A. Zeilinger, *Science* **2012**, *338*, 640.
[10] B.C. Hiesmayr, M.J.A. De Dood, W. Löffler, *Phys. Rev. Lett.* **2016**, *116*, 073601.
[11] L. Marrucci, C. Manzo, D. Paparo, *Phys. Rev. Lett.* **2006**, *96*, 163905.
[12] Y. Zhao, J. S. Edgar, G. D. M. Jeffries, D. McGloin, D. T. Chiu, *Phys. Rev. Lett.* **2007**, *99*, 073901.
[13] K. P. Marzlin, W. Zhang, E. Wright, *Phys. Rev. Lett.* **1997**, *79*, 4728.
[14] Y. Tada, W. Nie, M. Oshikawa, *Phys. Rev. Lett.* **2015**, *114*, 195301.
[15] I. V. Basistiy, V. Y. Bazhenov, M. S. Soskin, M. V. Vasnetsov, *Opt. Commun.* **1993**, *103*, 422.
[16] A. Ferrando, M. Zacares, M. Garcia-March, J. A. Monsoriu, P. F. de Cordoba, *Phys. Rev. Lett.* **2005**, *95*, 123901.
[17] A. Ferrando, *Phys. Rev. E* **2005**, *72*, 036612.
[18] A. Ferrando, M. Zacares, M. Garcia-March, *Phys. Rev. Lett.* **2005**, *95*, 043901.
[19] V. M. Pérez-García, M. A. García-March, A. Ferrando, *Phys. Rev. A* **2007**, *75*, 033618.
[20] A. Bezryadina, E. Eugenieva, Z. Chen, *Opt. Lett.* **2006**, *31*, 2456.
[21] A. Bezryadina, D. N. Neshev, A. Desyatnikov, J. Young, Z. Chen, Y. S. Kivshar, *Opt. Express* **2006**, *14*, 8317.
[22] N. Gao, C. Xie, *Opt. Lett.* **2012**, *37*, 3255.
[23] J. M. Hickmann, E. J. S. Fonseca, W. C. Soares, S. Chavez-Cerda, *Phys. Rev. Lett.* **2010**, *105*, 053904.
[24] M. Zacares, M. A. Garcıa-March, J. Vijande, A. Ferrando, E. Merino, *Phys. Rev. A* **2009**, *80*, 043812.
[25] A. Ferrando, M. A. Garcıa-March, *J. Opt.* **2013**, *15*, 044014.
[26] D. Novoa, I. J. Sola, M. A. Garcıa-March, A. Ferrando, *Appl. Phys. B* **2014**, *116*, 779.
[27] E. Brasselet, G. Gervinskas, G. Seniutinas, S. Juodkazis, *Phys. Rev. Lett.* **2013**, *111*, 193901.
[28] A. V. Kildishev, A. Boltasseva, V. M. Shalaev, *Science* **2013**, *339*, 1232009.
[29] M. Jang, Y. Horie, A. Shibukawa, J. Brake, Y. Liu, S. M. Kamali, A. Arbabi, H. Ruan, A. Faraon, C. Yang, *Nat. Photonics* **2018**, *12*, 84.
[30] N. Yu, F. Capasso, *Nat. Mater.* **2014**, *13*, 139.
[31] M. Khorasaninejad, W. T. Chen, R. C. Devlin, J. Oh, A. Y. Zhu, F. Capasso, *Science* **2016**, *352*, 1190.
[32] K. Ou, G. Li, T. Li, H. Yang, F. Yu, J. Chen, Z. Zhao, G. Cao, X. Chen, W. Lu, *Nanoscale* **2018**, *10*, 19154.
[33] D. Lin, P. Fan, E. Hasman, M. L. Brongersma, *Science* **2014**, *345*, 298.
[34] Y. Liu, Y. Ke, J. Zhou, Y. Liu, H. Luo, S. Wen, D. Fan, *Sci. Rep.* **2017**, *7*, 44096.
[35] F. Yue, D. Wen, J. Xin, B. D. Gerardot, J. Li, X. Chen, *ACS Photonics* **2016**, *3*, 1558.
[36] J. Zeng, L. Li, X. Yang, J. Gao, *Nano Lett.* **2016**, *16*, 3101.
[37] J. Zeng, T. S. Luk, J. Gao, X. Yang, *Sci. Rep.* **2017**, *7*, 11824.
[38] K. Zhang, X. Ding, L. Zhang, Q. Wu, *New J. Phys.* **2014**, *16*, 103020.
[39] K. Zhang, Y. Yuan, D. Zhang, X. Ding, B. Ratni, S. N. Burokur, M. Lu, K. Tang, Q. Wu, *Opt. Express* **2018**, *26*, 1351.
[40] X. Ni, S. Ishii, A. V. Kildishev, V. M. Shalaev, *Light: Sci. Appl.* **2013**, *2*, e72.
[41] X. Chen, L. Huang, H. Mühlenbernd, G. Li, B. Bai, Q. Tan, G. Jin, C. Qiu, S. Zhang, T. Zentgraf, *Nat. Commun.* **2012**, *3*, 1198.
[42] M. Khorasaninejad, W. T. Chen, A. Y. Zhu, J. Oh, R. C. Devlin, D. Rousso, F. Capasso, *Nano Lett.* **2016**, *16*, 4595.
[43] F. Aieta, P. Geneve, M. A. Kats, N. Yu, R. Blanchard, Z. Gaburro, F. Capasso, *Nano Lett.* **2012**, *12*, 4932.
[44] N. Yu, F. Aieta, P. Geneve, M. A. Kats, Z. Gaburro, F. Capasso, *Nano Lett.* **2012**, *12*, 6328.
[45] Y. Zhao, A. Alu, *Nano Lett.* **2013**, *13*, 1086.
[46] W. Cao, X. Yang, J. Gao, *Sci. Rep.* **2017**, *7*, 8841.
[47] H. Yang, G. Li, X. Su, G. Cao, Z. Zhao, F. Yu, X. Chen, W. Lu, *Opt. Express* **2017**, *25*, 16907.
[48] X. Ni, A. V. Kildishev, V. M. Shalaev, *Nat. Commun.* **2013**, *4*, 2807.
[49] L. Huang, X. Chen, H. Mühlenbernd, H. Zhang, S. Chen, B. Bai, Q. Tan, G. Jin, K. Cheah, C. Qiu, J. Li, T. Zentgraf, S. Zhang, *Nat. Commun.* **2013**, *4*, 2808.
[50] W. Wan, J. Gao, X. Yang, *Adv. Opt. Mater.* **2017**, *5*, 1700541.
[51] W. Wan, J. Gao, X. Yang, *ACS Nano* **2016**, *10*, 10671.
[52] G. Zheng, H. Mühlenbernd, M. Kenney, G. Li, T. Zentgraf, S. Zhang, *Nat. Nanotechnol.* **2015**, *10*, 308.
[53] Y. Guo, M. Pu, Z. Zhao, Y. Wang, J. Jin, P. Gao, X. Li, X. Ma, X. Luo, *ACS Photonics* **2016**, *3*, 2022.
[54] M. Pu, X. Li, X. Ma, Y. Ma, Z. Zhao, C. Wang, C. Hu, P. Gao, C. Huang, H. Ren, X. Li, F. Qin, J. Yang, M. Gu, M. H. Hong, X. Luo, *Sci. Adv.* **2015**, *1*, e1500396.
[55] G. Molina-Terriza, J. Recolons, J. P. Torres, L. Torner, E. M. Wright, *Phys. Rev. Lett.* **2001**, *87*, 023902.
[56] G. Molina-Terriza, E. M. Wright, L. Torner, *Opt. Lett.* **2001**, *26*, 163.
[57] J. E. Curtis, D. G. Grier, *Opt. Lett.* **2003**, *28*, 872.
[58] C. Yan, X. Li, M. Pu, X. Ma, F. Zhang, P. Gao, Y. Guo, K. Liu, Z. Zhang, X. Luo, *ACS Photonics* **2019**, *6*, 628.
[59] Y. Zhang, J. Gao, X. Yang, *Adv. Opt. Mater.* **2019**, *7*, 1801486.

 © 2019 WILEY-VCH Verlag GmbH & Co. KGaA, Weinheim